A precise mass measurement of PSR J2045 + 3633

J. W. McKee [1,2]★ P. C. C. Freire [1]★ M. Berezina,[1] D. J. Champion [1] I. Cognard,[3,4] E. Graikou,[1]
L. Guillemot,[3,4] M. J. Keith,[5] M. Kramer,[1,5] A. G. Lyne,[5] B. W. Stappers,[5] T. M. Tauris[6]★
and G. Theureau[3,4,7]

[1]*Max-Planck-Institut für Radioastronomie, Auf dem Hügel 69, D-53121 Bonn, Germany*
[2]*Canadian Institute for Theoretical Astrophysics, University of Toronto, 60 St. George Street, Toronto, ON M5S 3H8, Canada*
[3]*Laboratoire de Physique et Chimie de l'Environnement et de l'Espace LPC2E CNRS-Université d'Orléans, F-45071 Orléans, France*
[4]*Station de Radioastronomie de Nançay, Observatoire de Paris, CNRS/INSU, F-18330 Nançay, France*
[5]*Jodrell Bank Centre for Astrophysics, School of Physics and Astronomy, The University of Manchester, Manchester M13 9PL, UK*
[6]*Department of Physics and Astronomy, Aarhus University, Ny Munkegade 120, DK-8000 Aarhus C, Denmark*
[7]*Laboratoire Univers et Théories LUTh, Observatoire de Paris, PSL Research University, CNRS/INSU, Université Paris Diderot, 5 place Jules Janssen,
F-92190 Meudon, France*

ABSTRACT

We present the results of a timing analysis undertaken with the goal of obtaining an improved mass measurement of the recycled pulsar J2045 + 3633. Using regular high-cadence observations with the Effelsberg, Nançay, and Lovell radio telescopes, together with targeted campaigns with the Arecibo Telescope and Effelsberg, we have assembled a 6-yr timing data set for this pulsar. We measure highly significant values for the proper motion and the related rate of change of orbital semimajor axis ($\dot{x}$), and have obtained high-precision values of the rate of advance of periastron time ($\dot{\omega}$), and two of the Shapiro delay parameters (h_3 and ς). This has allowed us to improve the measurements of the pulsar and companion masses by an order of magnitude, yielding (with 1σ uncertainties) $1.251^{+0.021}_{-0.021}\,M_\odot$ for PSR J2045 + 3633, and $0.873^{+0.016}_{-0.014}\,M_\odot$ for its white dwarf companion, and has allowed us to place improved constraints on the geometrical orientation of the binary system. Using our measurements of the binary component masses and the orbital size, we consider possible evolutionary scenarios for the system.

Key words: stars: neutron – pulsars: general – pulsars: individual (PSR J2045 + 3633) – stars: rotation.

1 INTRODUCTION

1.1 Binary pulsar timing

The timing of radio pulsars, fast-spinning neutron stars (NSs), which emit a periodic train of radio pulses, is a powerful tool with a great variety of applications (see examples in Lorimer & Kramer 2005). For pulsars in binary systems, precise and continued timing has allowed for stringent tests of gravity theories (see e.g. Wex 2014 for a review), and detailed studies of the properties of NSs, in particular, their masses which are important for the study of superdense matter in their interiors (e.g. Özel & Freire 2016). This is possible as pulsar timing analyses of orbits can yield extremely precise measurements of the five Keplerian orbital parameters, measured from the radial motion of the pulsar and in the case of compact systems with a degenerate companion, small relativistic effects on the orbits and the propagation of the radio waves to the observer (Lorimer & Kramer 2005, and see Lorimer 2008 for a review). These relativistic perturbations (together with other non-Keplerian effects that arise from classical mechanics) can be parametrized in a theory-independent way by a set of 'Post-Keplerian' (PK) parameters (Damour & Taylor 1992). The detection of two PK parameters generally allows, under the assumption of a

relativistic theory of gravity, the measurement of the masses of the components of the binary system, and the measurement of additional PK parameters allows a self-consistency test of that gravity theory (see Stairs 2003, for a review).

This technique provided the first indirect detection of gravitational waves (GWs) in the late 1970s, from the observed orbital decay of the first-discovered binary pulsar, PSR B1913 + 16, the famous 'Hulse-Taylor' binary (Weisberg & Taylor 1981; Weisberg & Huang 2016; Damour 2015, and references therein). Pulsar timing analysis demonstrated that the measured orbital decay was shown to be in exact agreement with the general relativity (GR) prediction for the energy loss via emission of quadrupolar GWs. The same technique allowed five independent high-precision tests of GR in the 'double pulsar' system, using the faster-spinning first-formed pulsar (PSR J0737 − 3039A, Kramer et al. 2006). Other studies have strongly constrained alternative theories of gravity, in particular, by searching for effects arising from the violation of the strong equivalence principle (SEP). These include dipolar GW emission (see e.g. Freire et al. 2012, and also Shao et al. 2017; Anderson, Freire & Yunes 2019 for recent summaries) and a violation of the universality of free-fall (Archibald et al. 2018; Voisin et al. 2020). No SEP violation has been detected, and to date the results of all high-precision tests of gravity have been consistent with the predictions of GR.

This is useful for our purposes, because if we are confident that a particular binary pulsar has a degenerate companion, then in general classical Newtonian perturbations to the Keplerian orbital motion are

★ E-mail: jmckee@cita.utoronto.ca (JWM); pfreire@mpifr-bonn.mpg.de (PCCF); tauris@aias.au.dk (TMT)

absent. In this case, we can infer the component masses from only two PK parameters, by assuming that those parameters are as given by GR.

However, measuring two PK parameters is not trivial: At the time of writing, there are more than 300 known binary pulsars, of which only 38 have precise mass measurements based on this technique.[1] This is because the measurement of PK parameters depends on several factors, some of which are under our control, such as the length of the timing baselines and, to a lesser extent, the timing precision (which can be improved through the use of high-gain telescopes, the use of coherent dedispersion, the choice of optimal bands for observing, long integration times, and large bandwidths). Other factors are totally beyond our control, in particular, the intrinsic characteristics of the system: The flux density of the pulsar, its orbital period, eccentricity, inclination, and companion mass. All of these factors determine the magnitude and measurability of the PK parameters. For eclipsing binary pulsars in 'black widow' or 'redback' systems, relativistic perturbations are overwhelmed by the Newtonian effects in the orbits (e.g. Shaifullah et al. 2016), preventing the measurement of any PK parameters even under the best conditions.

Although the sample size is small compared to the known population, the number of NS mass measurements already yields impressive results. Some NS masses are measured to very high precision: e.g. PSR B1534 + 12 has a pulsar mass $m_p = 1.3330(2)\,M_\odot$ and a companion mass $m_c = 1.3455(2)\,M_\odot$, i.e. a precision $\sigma_m/m < 0.015$ per cent (Fonseca, Stairs & Thorsett 2014). Pulsars also show a range of masses much wider than thought until only a few years ago, from $1.174(4)\,M_\odot$ (Martinez et al. 2015) to $2\,M_\odot$ and above (Antoniadis et al. 2013; Cromartie et al. 2020).

1.2 Motivation and structure of this work

Increasing the number of precisely measured NS systems is useful for several reasons, which we consider here. First, statistical analyses of the distribution of masses throughout the known population (Antoniadis et al. 2016) suggest a bi-modal distribution, but more high-precision measurements are necessary to either confirm or disprove this finding. Secondly, precise NS masses are important for astrophysical studies, in particular the physics of supernovae. An important example of this is the apparent relation between the supernova kick and the mass of the resulting NS (Tauris et al. 2017). Thirdly, the maximum NS mass represents a fundamental constraint on the equation of state of neutron matter at densities above those of nuclear matter, a fundamental question in nuclear physics (Lattimer & Prakash 2001; Özel & Freire 2016).

The system described in detail in this work, PSR J2045 + 3633, is a 31.7-ms pulsar discovered by Berezina et al. (2017) as part of the HTRU-North pulsar survey (Barr et al. 2013). The measured spin period P and spin-down rate indicate that this pulsar is old (characteristic age $\tau_c = P/2\dot{P} \sim 800\,\mathrm{Myr}$), and is therefore part of the 'recycled' population of pulsars, which were spun up by accretion of matter from another star, the progenitor of their present companions (e.g. Alpar et al. 1982). In the same way, as most (but not all) recycled pulsars, it is in a binary system, with an orbital period of 32.3 d. From initial analysis following the discovery of the pulsar, the large mass function ($f = 0.10646\,M_\odot$) implied that the companion

is relatively massive. One of the unusual features of this system is its orbital eccentricity, $e \sim 0.017$. This is too small for the companion to be a second NS, as the sudden mass-loss via the supernova in which it formed would have resulted in a highly eccentric orbit (see e.g. Tauris et al. 2017), meaning the companion is more likely a white dwarf (WD). The companion mass is among the largest known for pulsar-WD systems. At the time of writing, there has been no attempt to detect the WD companion at optical wavelengths, but the large distance ($\sim$5.5 kpc) suggests that this would be difficult, while the combination of the large mass and old age implies that the WD has likely cooled to the extent that the brightness is below detectability limits.

Since its discovery, the characteristics of this system have made it a promising candidate for precise mass determination, and the combination of the large companion mass and high timing precision enabled Berezina et al. (2017) to detect the Shapiro delay (Shapiro 1964). The large orbital eccentricity also allowed the rate of advance of periastron ($\dot{\omega}$) to be measured and, assuming the validity of GR, they were able to combine both effects to measure masses of $1.33^{+0.30}_{-0.28}\,M_\odot$ for the pulsar and $0.94^{+0.14}_{-0.13}\,M_\odot$ for the companion. These values were not precise enough to be interesting from an astrophysical point of view, however, they made it clear that continued timing would yield much improved measurements of the PK parameters and therefore much more precise masses for the pulsar and the companion. In particular, with the Arecibo observations, they were able to achieve a timing precision well under 1 μs for the measurement of the topocentric pulse times of arrival (TOAs).

In the remainder of the paper, we will first (Section 2) describe the observations of PSR J2045 + 3633 used in this work, and how they were analysed. In Section 3, we will present our main timing results. We then discuss their astrophysical implications in Section 4. Finally, we summarize our findings in Section 5.

2 OBSERVATIONS AND DATA REDUCTION

Our data set comprises the observational data that were used in Berezina et al. (2017), as well as data obtained from continued monitoring and special campaigns undertaken for this study. The observations used in Berezina et al. (2017) were made with the Effelsberg Radio Telescope in Germany, The Nançay Radio Telescope in France, and the Lovell Telescope at Jodrell Bank in the United Kingdom, in addition to a dense orbital campaign undertaken with the Arecibo Telescope in the United States.

For this work, we have included an additional four years of data from regular monitoring with the Effelsberg, Nançay, and Lovell telescopes, at cadences of approximately 1 month, 14 d, and 10 d, respectively. We also include data taken during two special campaigns: one with Effelsberg and one with Arecibo, conducted with a view to obtaining a precise measurement of the Shapiro delay. The observational setup of the telescopes used in this work is summarized in Table 1.

At the Effelsberg telescope, PSR J2045 + 3633 is observed approximately monthly as part of an ongoing key science project to monitor a number of relativistic pulsar binaries. Observations with the Effelsberg telescope used two receivers: a single-pixel receiver with a centre frequency of 1347.5 and 200 MHz of bandwidth (observations prior to 2017), and a multibeam receiver with a centre frequency of 1397.5 and 400 MHz of bandwidth (2017 onward). In the case of both receivers, data recording used the ROACH-based PSRIX backend with coherent-dedispersion, detailed in Lazarus et al. (2016). In addition to the regular monitoring, a special campaign took place between July and August 2019, and used scans lasting between

---

[1]We define 'precise' as a pulsar mass m_p measured to 15 per cent relative uncertainty. See https://www3.mpifr-bonn.mpg.de/staff/pfreire/NS_masses.html

Table 1. Summary of the configurations used in our observations of PSR J2045 + 3633.

Telescope	Backend	Centre frequency (MHz)	Bandwidth (MHz)	Date range	MJD range
Effelsberg (single-pixel receiver)	PSRIX	1347.5	200	2014-12-5–2016-12-13	56996–57735
Effelsberg (multibeam receiver)	PSRIX	1397.5	400	2017-5-13–2019-9-13	57886–58739
Nançay	NUPPI	1484	512	2015-3-16–2020-7-13	57097–59043
Lovell	ROACH	1520	384	2014-9-14–2020-2-23	56914–58902
Arecibo (first campaign)	PUPPI	1431	700	2015-8-24–2015-9-29	57258–57294
Arecibo (second campaign)	PUPPI	1381	800	2019-9-19–2019-11-4	58745–58791
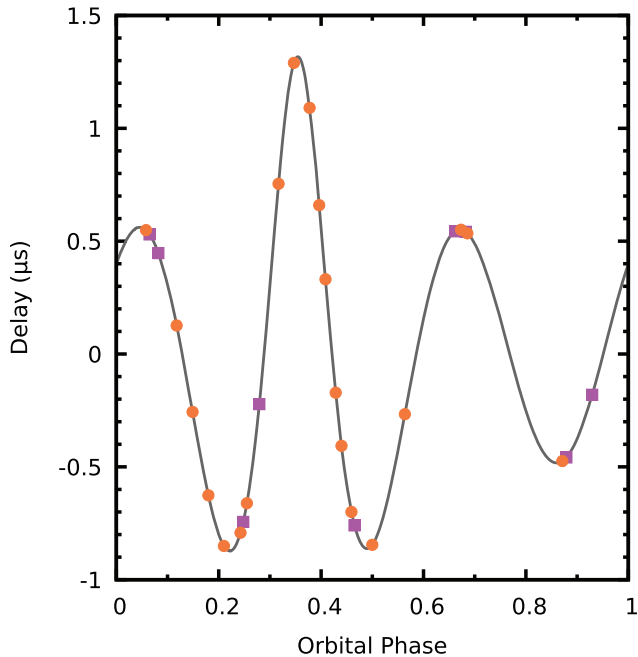
Figure 1. Diagram of the PSR J2045 + 3633 orbital phase relative to periastron showing the harmonic decomposition of the unabsorbed Shapiro delay signal (see the text), and highlighting the observations taken during our two targeted campaigns with Effelsberg (orange circles) and Arecibo (purple squares). Observations with both telescopes were scheduled to be close to the local minima and maxima of the Shapiro delay signal, allowing our sensitivity to the overall shape of the signal to be maximized. Longer scans with Effelsberg were used close to the global maximum, to improve our sampling of this part of the orbit.

1.5 and 3.5 h, totalling ∼45 h. A higher cadence of observations was used at orbital phases corresponding to local maxima and minima of the harmonic decomposition of the unabsorbed Shapiro delay signal, calculated from equation (28) of Freire & Wex (2010), with particular focus on the global maximum, with the goal of placing better constraints on the Shapiro delay signal, rather than when solely focusing on the maximum delay corresponding to the superior conjunction (Fig. 1).

The Lovell observations were taken using a receiver working in the frequency range 1300–1700 MHz, with a maximum usable bandwidth of 400 MHz, and acquired using a ROACH system detailed in Bassa et al. (2016). Observations of PSR J2045 + 3633 are taken approximately every two weeks, as part of the Jodrell Bank monitoring programme of ∼800 pulsars in the Northern Sky.

The Nançay Radio Telescope observations used a 1484-MHz receiver with 512 MHz of bandwidth, and recorded with a dedispersing

ROACH backend (NUPPI[2]), which is described in Liu et al. (2014). PSR J2045 + 3633 is observed approximately every 10 d with the Nançay Radio Telescope, as part of a campaign to provide high-cadence monitoring of >100 recycled pulsars.

Our Arecibo Telescope data set is made up of two targeted campaigns. The first was taken in late 2015, and is presented in Berezina et al. (2017). Observations from the first campaign used a centre frequency of 1431 MHz and a bandwidth of 700 MHz, and were coherently dedispersed. The second campaign was undertaken specifically for this work, and took place between September and November 2019. The observation dates were chosen to sample the turning points of the harmonic decomposition of the Shapiro delay signal (although not the maximum, due to missed observations), which we illustrate in Fig. 1. A centre frequency of 1381 MHz and a bandwidth of 800 MHz was used. Observations used scans of approximately 1 h in length, with the entire campaign totalling ∼13 h. Fig. 2 shows the pulse profile obtained during one such observing scan.

The observations from all telescopes were refolded with the same ephemeris (adapted from the one presented in Berezina et al. 2017), and coherently dedispersed with the same dispersion measure (DM). In the case of Effelsberg, Nançay, and Arecibo, polarization calibration was applied, using noise diode scans that took place immediately before the observations, of lengths 2–5 min (Effelsberg and Arecibo) and 10 s (Nançay). The data were also corrected for rotation measure, using the value measured by Berezina et al. (2017). Observations were manually inspected for RFI, with channels and sub-integrations badly affected by RFI being masked, using the PAZI tool from PSRCHIVE[3] (Hotan, van Straten & Manchester 2004).

Often in high-precision timing studies of pulsars, TOAs are generated for several sub-bands across the total observing bandwidth, with the purpose of measuring and removing the dispersive delay due to the interstellar medium (e.g. Alam et al. 2020), or to give greater weighting to parts of the band that have been enhanced in flux by interstellar scintillation. Until recently, this approach would typically use a single template, created from the frequency-averaged total bandwidth, to generate a TOA from each frequency channel. Some pulsars, including PSR J2045 + 3633, display significant profile evolution across wide observing bandwidths, meaning that a single template will not optimally describe the pulse shape in each channel. In this case, an additional set of parameters (known as FD parameters) are required to be fit in the timing model to account for the additional fixed phase delays per channel (see e.g. Alam et al. 2020). In our analysis, we instead use frequency-resolved templates to improve timing precision when compared to the single-template case, and to remove the requirement of fitting a set of FD parameters in the timing model.

For our frequency-resolved timing, we followed the approach detailed by Donner et al. (2019), who employed this technique on LO-

---

[2]https://github.com/gdesvignes/NUPPI
[3]http://psrchive.sourceforge.net/
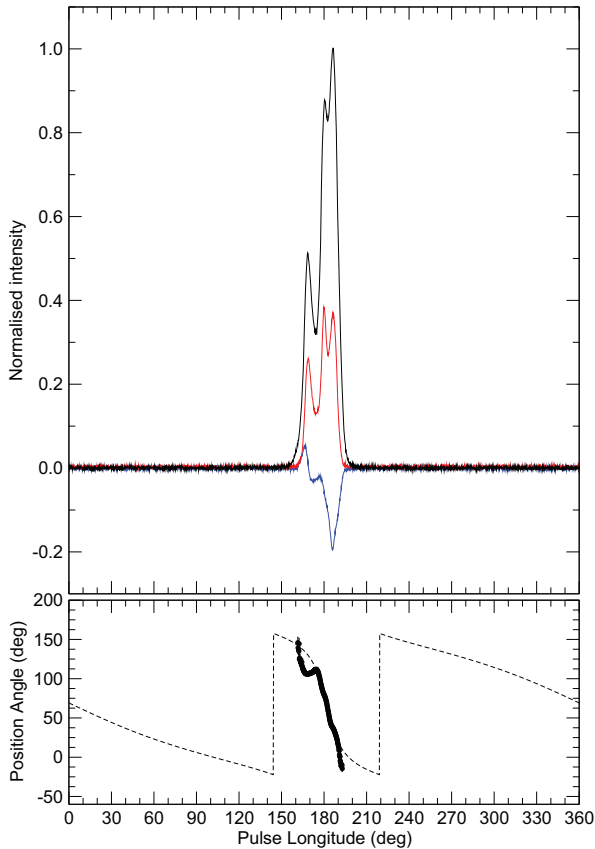
Figure 2. The pulse profile of PSR J2045 + 3633, obtained from a 62-min scan with the Arecibo Telescope at 1431 MHz (700-MHz bandwidth). The observational data were polarization calibrated, corrected for Faraday rotation, and then fully integrated in time and observing frequency. The top panel shows the total intensity (Stokes *I*, black line), the corresponding linearly polarized intensity (Stokes *L*, red line), and the circularly polarized intensity (Stokes *V*, blue line). The signal-to-noise ratio (S/N) of this observation is approximately 3000. The lower panel shows the position angle (PA) of the linearly polarized emission. The dashed line shows a modelling of the PA values within the Rotating Vector Model (RVM, see the text for details.).

FAR and GLOW observations of pulsars at frequencies <150 MHz, where intrinsic profile evolution with frequency is very rapid, and extrinsic frequency-dependent effects such as scattering and DM variations are highly significant. We made high-S/N reference profiles for each telescope by summing the top 10 per cent highest S/N observations from each, after fully integrating in observation time and polarization, to increase S/N and reduce correlated noise. These reference templates were then integrated to have 100-MHz channel widths in the case of Effelsberg, Lovell, and Arecibo, and 128 MHz in the case of Nançay. A wavelet smoothing algorithm was then applied to each channel, to further increase S/N. We then integrated our data sets in frequency so that the same channel widths as the templates were used, and with 10-min sub-integration times. From these, TOAs were generated by cross-correlating the observational data with the frequency-resolved reference templates, using a Fourier domain Markov chain Monte Carlo algorithm included in the PAT tool in PSRCHIVE. Our timing data set is summarized in Table 2.

Our timing analysis follows the standard techniques that have been used extensively in studies such as this (see e.g. Desvignes et al. 2016). The TOAs from each unique telescope and receiver

system were aligned by fitting for time offsets. DM variations were modelled using a Taylor series, with higher order terms being added until the χ^2 of the resulting fit was reduced by less than one, which resulted in a third-order Taylor series for the final DM model. For each of these data sets, the uncertainties were scaled by a constant factor ('EFAC' in Table 2) such that the post-fit reduced $\chi^2 = 1$. We used the TEMPO[4] pulsar timing software for our analysis, and we present our timing residuals (i.e. the difference between observed TOAs and our timing model) in Fig. 3.

Our analysis of the binary parameters started from the timing model presented in Berezina et al. (2017). This was adapted to derive new timing models, which are extensions of the theory-independent DD model (Damour & Deruelle 1985,1986). The first is the DDGR model, which assumes the validity of GR and fits self-consistently for the masses of the components in the binary system. The second is the DDFWHE model, which includes the orthometric re-parametrization of the Shapiro delay (Freire & Wex 2010); this was implemented in TEMPO by Weisberg & Huang (2016). Finally, the DDK model (extended to include kinematic effects, Kopeikin 1995,1996) was used to calculate χ^2 maps of the binary parameter space (discussed in the next section). All analyses used the DE435 planetary ephemeris (Folkner et al. 2016) to correct for the motion of the radio telescope relative to the Solar system barycentre.

3 RESULTS

Our timing analysis resulted in the measurements of the timing parameters presented in Tables 3 and 4. In the latter Table, we present the results of two models: one that assumes the validity of GR (the DDGR model), and a theory-independent model (the DDFWHE model). We also present there the results of the χ^2 mapping we have carried out using the DDK model. All parameters are expressed in Dynamic Barycentric Time (TDB), the spin and astrometric parameters refer to the reference epoch listed, and the orbital parameters are valid for the time of passage through periastron listed (T_0). All parameters are quoted with 1σ confidence limits. The timing residuals (i.e. the measured TOAs minus the DDGR model prediction for their respective rotation numbers) are presented in Fig. 3, which demonstrates that the TOAs are well described by the models in Tables 3 and 4.

In what follows, we present a discussion on the different timing parameters in these tables.

3.1 Proper motion and distance

One of the new results from this work is a high-precision measurement of the proper motion PSR J2045 + 3633. We measure the total proper motion to be 4.17(6) mas yr^{-1}, with a PA of the proper motion (Θ_μ) of 230.1(8)° in J2000 coordinates and 281.2(8)° in Galactic coordinates. The convention used here for the PA is the so-called 'observer's convention', where a PA of 0° indicates North, and 90° indicates East. In Galactic coordinates, the horizontal and vertical components of its motion are given by -4.1 and $+0.8$ mas yr^{-1}, respectively. The first minus sign indicates a Westwards motion in the Galaxy, i.e. in a sense of decreasing Galactic longitude *l*. The second plus sign means the pulsar is increasing its Galactic latitude *b*, i.e. it is slowly approaching the Galactic plane.

In order to calculate the heliocentric velocity, we must have an estimate of the distance to the system, *d*. We do not detect

---

[4]http://tempo.sourceforge.net/

Table 2. Summary of our timing data set used in this work. The final column refers to the weighted RMS of the post-fit timing residuals with the DDGR model.

Data set	TOA integration time (s)	TOA Bandwidth (MHz)	N_{TOA}	EFAC	W_{RMS} (µs)
Effelsberg (single-pixel receiver)	600	100	166	1.042	5.57
Effelsberg (multibeam receiver)	600	100	1016	1.069	6.79
Nançay	600	128	1672	1.358	11.13
Lovell	600	100	1966	1.018	16.63
Arecibo (first campaign)	600	100	196	1.920	2.23
Arecibo (second campaign)	600	100	343	1.150	1.79
All	–	–	5359	–	5.52

a parallax signal from the pulsar timing, and we instead use an estimated distance from two Galactic electron density models: NE2001 (Cordes & Lazio 2002) and YMW16 (Yao, Manchester & Wang 2017). These models use the observed DM of a series of pulsars with independent distance measurements (e.g. parallax from timing or VLBI) to estimate the free electron density along particular lines of site, i.e.

$$\text{DM} = \int_0^d n_e \, dl. \tag{1}$$

These models only represent a crude estimate, particularly for distant pulsars, where independent distance measurement are difficult to obtain for that part of the Galaxy. We therefore assign a conservative estimate of the distance uncertainty of 20 per cent, take the distance values as $d_{\text{NE2001}} = 5.5(11)$ kpc and $d_{\text{YMW16}} = 5.6(11)$ kpc. These estimates are mutually consistent. For the remainder of the calculations, we use the NE2001 estimate with the 20 per cent distance uncertainty.

The NE2001 distance and its 20 per cent uncertainty implies a Heliocentric velocity of 109(22) km s^{-1}. This is only a basic estimate of the dynamics of the system, and we will present a more detailed analysis of the motion of the system in Section 4.

3.2 Keplerian parameters and the mass function

The five Keplerian parameters measured to high-precision in all binary pulsar systems are the orbital period (P_b), the semimajor axis of the pulsar's orbit projected along the line of sight (x), the orbital eccentricity (e), the longitude of periastron (ω), and the time of passage through periastron (T_0). The first two yield the mass function from Kepler's third law:

$$f(m_p, m_c) = \frac{(m_c \sin i)^3}{M^2} = \frac{4\pi^2}{T_\odot} \frac{x^3}{P_b^2} = 0.10\,646\,016(3)\,\text{M}_\odot, \tag{2}$$

where $M = m_p + m_c$ is the total mass of the system, m_p and m_c are the masses of the pulsar and companion, respectively, i is the orbital inclination angle, and $T_\odot = G\text{M}_\odot c^{-3} = 4.925\,490\,947\,641\,267\,\mu\text{s}$ is a constant describing the speed of light traveltime across a 1 M$_\odot$ gravitational radius (here, G is the gravitational constant, and c is the speed of light; since the factors G, M$_\odot$, and c are defined exactly, $T_\odot$ is also an exact constant). As x and P_b are usually measurable to high precision, the mass function is often very well known. However, measurements of other quantities are required to disentangle m_p and m_c.

3.3 Rate of advance of periastron

From our timing analysis, we have greatly improved the measurement of the rate of advance of periastron, yielding the value $\dot{\omega} = 0.001\,009(10)^\circ$ yr^{-1}. In the absence of other nearby (i.e.

gravitationally-interacting) objects, this is given by

$$\dot{\omega}_{\text{obs}} = \dot{\omega}_{\text{rel}} + \dot{\omega}_k + \dot{\omega}_{\text{SO}}. \tag{3}$$

The first term is the relativistic periastron advance. Assuming that GR is the correct theory of gravity, this is given by (Taylor & Weisberg 1982)

$$\dot{\omega}_{\text{rel}} = 3T_\odot^{2/3} \left(\frac{P_b}{2\pi}\right)^{-5/3} \frac{1}{1-e^2} M^{2/3}. \tag{4}$$

From our measured value of $\dot{\omega}$, we obtain a total mass of 2.14(3) M$_\odot$. This constraint on the total mass is represented by the red lines in Fig. 4.

The second term, $\dot{\omega}_k$, is the kinematic contribution. This becomes important for several binary systems that have orbital periods similar to those of PSR J2045 + 3633 (Freire et al. 2011; Stovall et al. 2019), and is given by (Kopeikin 1996)

$$\dot{\omega}_k = \frac{\mu_T}{\sin i} \cos(\Theta_\mu - \Omega), \tag{5}$$

where $\mu_T = \sqrt{\mu_\alpha^2 + \mu_\delta^2}$ is the total pulsar proper motion (i.e. the magnitude of the proper motion in right ascension and declination components, α and δ), Θ_μ is the PA of the proper motion, and Ω is the PA of the orbital line of nodes. For PSR J2045 + 3633, we can derive maximum and minimum limits (i.e. when the proper motion is orthogonal to the line of nodes) for this effect from the estimate of i in Table 4 and the measured proper motion. From this, we obtain $|\dot{\omega}_k| \leq 1.4 \times 10^{-6\circ}$ yr^{-1}. This is smaller than the measurement uncertainty of $\dot{\omega}$, which is approximately $10^{-5\circ}$ yr^{-1}. This means that the uncertainty on the total mass of the system is still dominated by the measurement uncertainty for $\dot{\omega}$.

The final term in equation (3) arises from the spin-orbit coupling of the system, and is negligible in the case of PSR J2045 + 3633. We discuss this in detail in Section 3.7.

Since M is known, we can immediately estimate the orbital separation, a, from Kepler's third law

$$\frac{a}{c} = \left[MT_\odot \left(\frac{P_b}{2\pi}\right)^2 \right]^{1/3} = 127.6(6)\,\text{lt-s.} \tag{6}$$

This value is independent of the orbital inclination i, and the uncertainty is dominated by the uncertainty in M. We comment on the implications of this value in Section 4.3.

3.4 Shapiro delay

Our dense observations made around superior conjunction have allowed us to make improved measurements of the Shapiro delay parameters in this system. In the DD orbital model, the Shapiro delay is characterized by two PK parameters: the range (r) and shape (s).
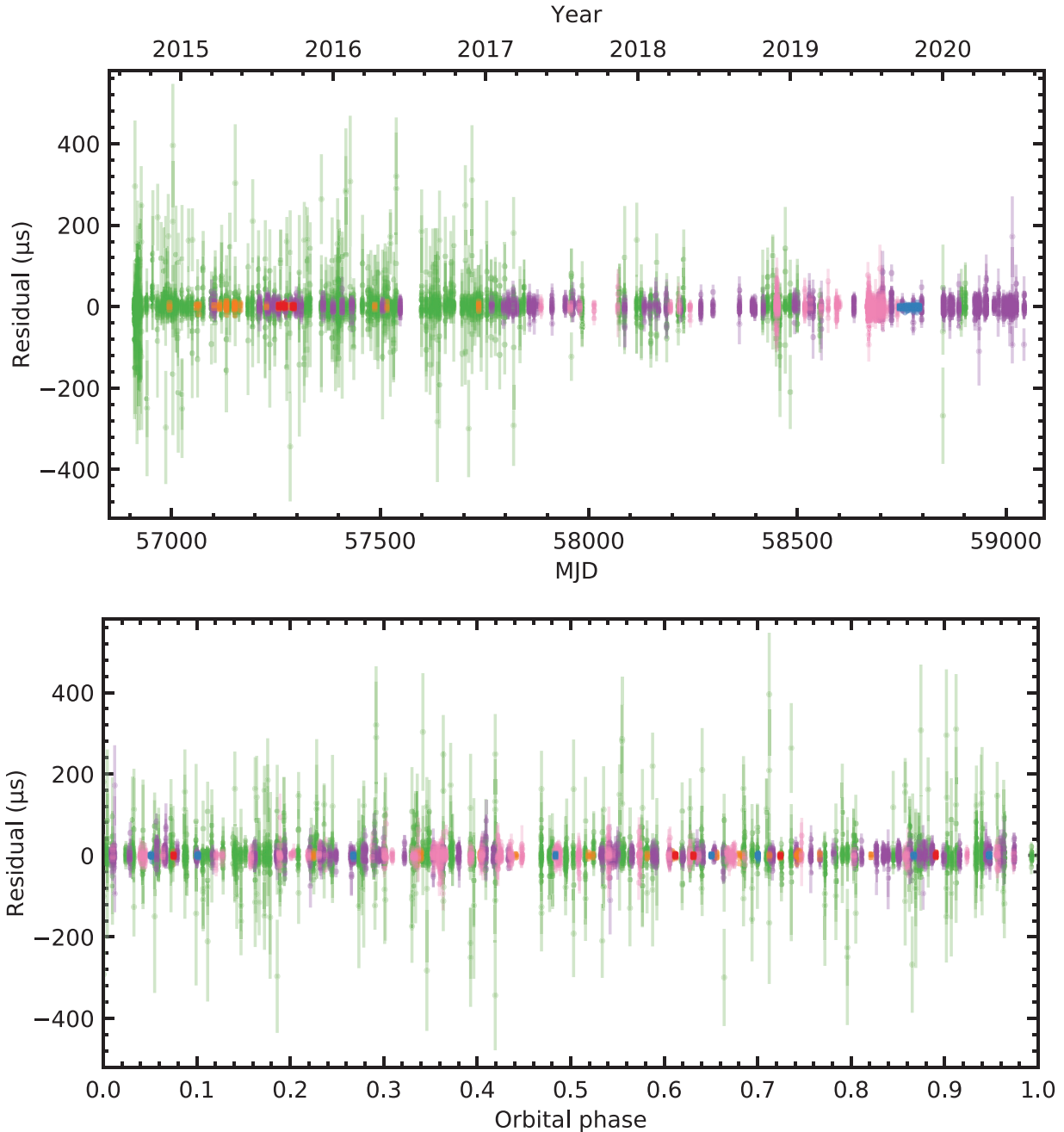
Figure 3. PSR J2045 + 3633 timing residuals, plot as a function of MJD (above) and orbital phase relative to periastron, and analysed using the DDGR orbital model (see the text). Data up to MJD 57538 were included in Berezina et al. (2017). The weighted RMS of the timing residuals is 5.52 μs. The following colour coding is used: Lovell (green), Nançay Radio Telescope (purple), Effelsberg Telescope single-pixel (orange), Effelsberg Telescope multibeam (pink), Arecibo Telescope 1431 MHz (red), and Arecibo Telescope 1381 MHz (blue).

In GR, these relate to the masses and orbital inclinations according to the following expressions:

$$r = \frac{Gm_c}{c^3} = T_\odot m_c, \tag{7}$$

$$s = \sin i = T_\odot^{-1/3} \left(\frac{P_b}{2\pi}\right) x \frac{(m_p + m_c)^{2/3}}{m_c}. \tag{8}$$

For most systems, particularly those with low orbital inclinations, the r and s parameters are strongly correlated. For such systems, it is better to use an alternative set of PK parameters: the orthometric

amplitude (h_3) and ratio (ς), respectively (Freire & Wex 2010), to describe the Shapiro delay. These are given by

$$\varsigma = \frac{\sin i}{1 + \sqrt{1 - \sin^2 i}} = \tan\left(\frac{i}{2}\right), \tag{9}$$

$$h_3 = r\varsigma^3. \tag{10}$$

The orthometric parameters do not yield better mass measurements, but they are less correlated with each other and therefore provide a better description of the regions of the $\cos i$–m_c plane where the system is most likely to be located. Our measurements yield

Table 3. PSR J2045 + 3633 spin and astrometric parameters measured from our timing analysis, and associated quantities derived from them.

Observation and data reduction parameters	
Solar system ephemeris.................................	DE435
Reference epoch (MJD).................................	56 855.0
Solar wind electron number density, n_0 (cm^{-3}).................................	7.0
Spin and astrometric parameters	
Right ascension, α (J2000, h:m:s).................................	20:45:01.50510(2)
Declination, δ (J2000, d:m:s).................................	36:33:01.4046(2)
Proper motion in α, μ_α (mas yr^{-1}).................................	$-3.20(6)$
Proper motion in δ, μ_δ (mas yr^{-1}).................................	$-2.68(6)$
Spin frequency, ν (Hz).................................	31.563 820 566 264(3)
Spin-down rate, $\dot\nu$ (10^{-16} Hz s^{-1}).................................	$-5.8628(3)$
Dispersion measure, DM (cm^{-3} pc).................................	129.533(2)
First derivative of DM, DM1 (10^{-3} cm^{-3} pc yr^{-1}).................................	$+6.1(16)$
. . . DM2 (10^{-3} cm^{-3} pc yr^{-2}).................................	$-7.6(7)$
. . . DM3 (10^{-3} cm^{-3} pc yr^{-3}).................................	$+3.8(2)$
Rotation measure, RM (rad m^{-2}).................................	$-266(10)^a$
Derived parameters	
Galactic longitude, l ($°$).................................	77.8 323 570(2)
Galactic latitude, b ($°$).................................	$-3.925 76 397(7)$
Total proper motion, μ_T (mas yr^{-1}).................................	4.17(6)
PA of proper motion (J2000), Θ_μ ($°$).................................	230.1(8)
PA of proper motion (Galactic), Θ_μ ($°$).................................	281.2(8)
DM-derived distance (NE2001), d (kpc).................................	$5.5(11)^b$
DM-derived distance (YMW16), d (kpc).................................	$5.6(11)^b$
Parallax, $\bar\omega$ (mas).................................	0.18^c
Galactic height, z (kpc).................................	-0.381^c
Heliocentric transverse velocity, v_T (km s^{-1}).................................	$109(22)^c$
Spin period, P_0 (ms).................................	31.681 842 757 300(3)
Spin period derivative, $\dot P$ (10^{-19} s s^{-1}).................................	5.8847(3)
Total kinematic contribution to period derivative, $\dot P_k$ (10^{-19} s s^{-1}).................................	-0.074
Intrinsic spin period derivative, $\dot P$ (10^{-19} s s^{-1}).................................	$5.953^{+0.001}_{-0.005}$
Surface magnetic field strength, B_{surf} (10^9 G).................................	4.4
Characteristic age, τ_c (Gyr).................................	0.84
Spin-down power, $\dot E$ (10^{32} erg s^{-1}).................................	7.4

^{a}Obtained from Berezina et al. (2017).
^{b}Assuming a 20% uncertainty.
^{c}Assuming DM-derived distance (NE2001).

highly significant estimates for these parameters: $h_3 = 1.01(11)\,\mu$s and $\varsigma = 0.62(9)$. The GR mass constraints corresponding to these parameters are represented by the blue solid and dashed lines in Fig. 4. As we can see there, all three PK parameters converge at a consistent set of masses, within our measurement uncertainties. This represents, formally, a successful test of GR, however, the low precision of the masses provided by our Shapiro delay alone reduces the interest of this test.

Our mass measurements imply, using equation (2), an orbital inclination of either $63(2)°$ or $180° - 63(2)° = 117(2)°$. Within the uncertainties (discussed in detail below), the first value is consistent with the estimate of $i \sim 60°$ made by Berezina et al. (2017) for this system based on an RVM (Radhakrishnan & Cooke 1969) fit to polarization data of the pulsar. We have performed a similar RVM fit to the PAs measured as shown in Fig. 2. Due to the much higher S/N of the Arecibo data, the uncertainties in our PA values are much smaller than those of Berezina et al. (2017), and in order to obtain a suitable fit (shown by the dashed line in Fig. 2), we increased the uncertainties by a factor of 10. The result suggests a viewing angle $\zeta = 131^{+30}_{-23}°$, whereas the large uncertainties are not surprising given the relatively short longitude range that is available for the RVM fit

(cf. Lorimer & Kramer 2005). This implies an orbital inclination angle $i = 49^{+23}_{-30}°$ (see the discussion in Kramer et al. submitted), which is both consistent with the result of Berezina et al. (2017) and the solution for the Shapiro delay that favours $i = 63(2)°$.

3.5 Variation of the projected semimajor axis

In addition to the large improvements in precision to the parameters reported by Berezina et al. (2017), we have measured a significant variation in the orbital semimajor axis, $\dot x = -8.7(28) \times 10^{-15}$ lt-s s^{-1}. This allows us to impose a further constraint on the orbital geometry of the system.

The observed $\dot x$ is composed of a combination of intrinsic, geometric, and kinematic effects

$$\left(\frac{\dot x}{x}\right)^{obs} = \left(\frac{\dot x}{x}\right)^{k} + \left(\frac{\dot x}{x}\right)^{GW} + \frac{d\epsilon_A}{dt} - \frac{\dot D}{D} + \left(\frac{\dot x}{x}\right)^{\dot m} + \left(\frac{\dot x}{x}\right)^{SO},$$

(11)

where the terms in the above equation describe the contributions from the kinematic effects, shrinking of the orbit due to GW emission, aberration, the variation of the Doppler shift, radiative mass-loss,

Table 4. PSR J2045 + 3633 binary parameters measured from our timing analysis, with values separated by orbital model (see the text). Square brackets indicate derived quantities that are not directly measured. The results of the χ^2 mapping produce degenerate solutions for the orbital geometry, and so two values for i and four for Ω are listed.

Binary model..................................	DDGR	DDFWHE	DDK χ^2 grid
Keplerian orbital parameters			
Orbital period, P_b (d).................................	32.29784 447(8)	32.29 78 4 448(8)	–
Projected semimajor axis of the pulsar orbit, x (lt-s).................................	46.940 800(5)	46.940 797(4)	–
Epoch of periastron, T_0 (MJD).................................	57496.750 854(3)	57496.750 850(7)	–
Orbital eccentricity, e.................................	0.01721 2447(6)	0.01 721 245(2)	–
Longitude of periastron, ω (°).................................	320.77 788(3)	320.77 783(8)	–
Orbital inclination, i (°).................................	[63]	64(7)	$63.8^{+1.5}_{-1.6}$, $117.5^{+1.6}_{-1.5}$
PA of the orbital line of nodes, Ω (°)...........	–	–	9^{+13}_{-20}, 92^{+16}_{-13}, 187^{+13}_{-18}, 272^{+16}_{-13}
PK orbital parameters			
Shapiro delay 'shape', s.................................	[0.8 932 797]	0.90(6)	–
Rate of advance of periastron, $\dot{\omega}$ (° yr^{-1}).................................	[0.0010 074]	0.001 009(10)	–
Orbital period derivative, $\dot{P}_b$ (10^{-12} s s^{-1}).................................	3.5(53)	3.6(53)	–
Rate of change of orbital semimajor axis, $\dot{x}$ (10^{-15} lt-s s^{-1}).................................	−9.6(28)	−8.7(28)	–
Orthometric amplitude of the Shapiro delay, h_3 (μs).................................	–	1.01(11)	–
Orthometric ratio of the Shapiro delay, ς.................................	–	0.62(9)	–
Mass measurements			
Mass function, f (M$_\odot$).................................	0.10646 016(3)	0.106 46 014(3)	–
Total mass, M (M$_\odot$).................................	2.14(3)	[2.1353]	$2.127^{+0.031}_{-0.031}$
Pulsar mass, m_p (M$_\odot$).................................	1.26(3)	[1.2453]	$1.251^{+0.021}_{-0.021}$
Companion mass, m_c (M$_\odot$).................................	0.88(1)	0.9(4)	$0.873^{+0.016}_{-0.014}$

and spin-orbital coupling, respectively (these are described in detail in Lorimer & Kramer 2005). The spin-orbit coupling term was recently detected for the first time in a double-degenerate system, PSR J1141 − 6545 (Venkatraman Krishnan et al. 2020). We discuss the Newtonian and relativistic contributions of the spin-orbital coupling in detail in Section 3.7, and conclude that is is not of importance for this study.

A detailed analysis of the components of equation (11) shows that, for PSR J2045 + 3633, only the first term is important. This term describes the kinematic contribution, arising from the secular change of the orbital inclination angle due to the proper motion of the pulsar (Kopeikin 1996):

$$\left(\frac{\dot{x}}{x}\right)^k = \mu_T \cot i \sin(\Theta_\mu - \Omega).$$ (12)

The constraints introduced by our measurement of $\dot{x}$ are displayed by the solid orange lines in Fig. 5.

3.6 Variation of the orbital period

The observed spin period derivative and orbital period derivative consist of their variations in the reference frame of the centre of mass of the system (i.e. their intrinsic variations), with additional contributions from the acceleration due to the transverse velocity of the pulsar (the Shklovskii effect, Shklovskii 1970), and the difference of the Galactic accelerations of the Solar system and the binary pulsar projected along the line of sight to the binary pulsar (e.g. Lazaridis et al. 2009):

$$\left(\frac{\dot{P}_b}{P_b}\right)^{obs} = \left(\frac{\dot{P}_b}{P_b}\right)^{int} + \left(\frac{\dot{P}_b}{P_b}\right)^{Shk} + \left(\frac{a}{c}\right)^{Gal} + \left(\frac{a}{c}\right)^z.$$ (13)

What follows is a brief description of each of the terms in equation (13). The first term, the intrinsic $\dot{P}_b$, is made up of several effects, although in this case, the dominant effect is the orbital decay caused by the emission of GWs (Peters & Mathews 1963):

$$\dot{P}_b^{GW} = -\frac{192\pi}{5} T_\odot^{5/3} \left(\frac{P_b}{2\pi}\right)^{-5/3} f(e) \frac{m_p m_c}{(m_p + m_c)^{1/3}},$$ (14)

where $f(e)$ is the mass function in terms of orbital eccentricity, given by

$$f(e) = \frac{1 + (73/24)e^2 + (37/96)e^4}{(1 - e^2)^{7/2}}.$$ (15)

This effect mostly becomes significant in very close orbits consisting of compact objects. For our measured masses of PSR J2045 + 3633 and its companion, and assuming that GR is the correct theory of gravity, we obtain $\dot{P}_b^{GW} = -5.74(15) \times 10^{-17}$ s s^{-1}. This is negligible compared to our measurement precision. The same is true for other terms that contribute to $\dot{P}_b^{int}$, such as the variation of the orbital period due to radiative mass-loss in the system.
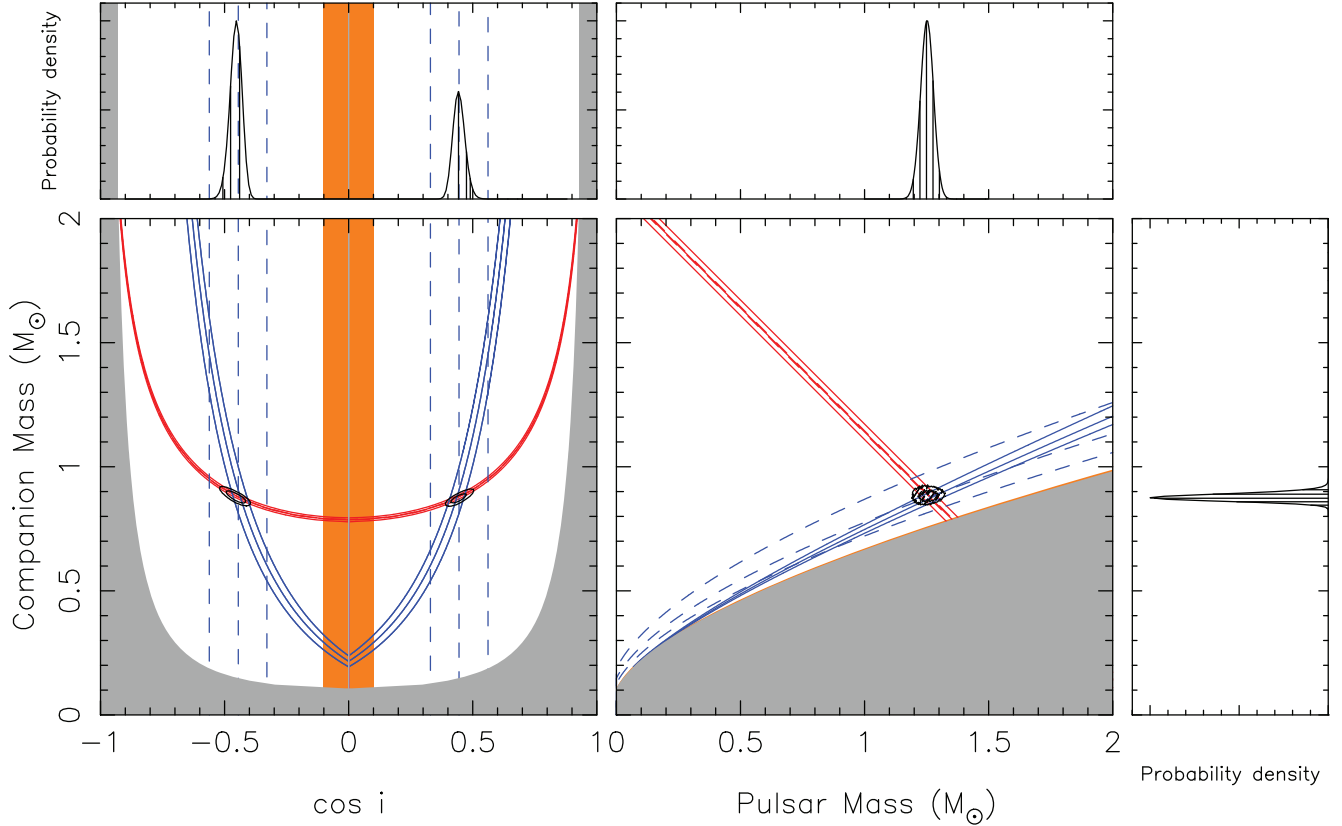
The Shklovskii effect arises from the total proper motion μ_T:

$$\left(\frac{\dot{P}_b}{P_b}\right)^{Shk} = \frac{\mu_T^2 d}{c}.$$ (16)

From this, we estimate the Shklovskii contribution to $\dot{P}_b$ to be $1.37(28) \times 10^{-13}$ s s^{-1}.

For a pulsar at a distance $D \equiv R_0/\delta$, the component of its acceleration due to the differential disc rotation around the Galactic

Figure 4. Mass constraints of the PSR J2045+3633 companion as a function of the cosine of the orbital inclination (left-hand panel), and of the PSR J2045 + 3633 mass (right-hand panel). The grey regions are excluded by the requirement that m_p is greater than zero (left-hand panel), and by our measurement of the mass function of the system (right-hand panel), and the orange region is excluded by our $\dot{x}$ measurement. The curves and 1σ uncertainty regions of the PK parameters measured with the DDGR orbital model are overplot; these are $\dot{\omega}$ (solid red), h_3 (solid blue), and ς (dashed blue). The contours show the 1σ and 2σ likelihood regions, measured from the χ^2 mapping with the DDK model, and the marginal probability densities are displayed for each plot axis. The values from both the timing with the DDFWHE model and the χ^2 mapping agree very well with each other, with all constraints being consistent with the 1σ uncertainty regions. The exact orbital inclination is not well-constrained: although the negative value of $\cos i$ is preferred, the polarimetry of the pulsar suggests that the positive $\cos i$ (with inclinations around $63°$) is the real value. The pulsar and companion masses are very well constrained, yielding values $m_p = 1.251^{+0.021}_{-0.021}$ M$_\odot$ and $m_c = 0.873^{+0.016}_{-0.014}$ M$_\odot$. The 1D probability density function for $\cos i$ is significantly narrower than the uncertainty for ς, the reason for that is the additional constraints for the inclination given by the measurement of $\dot{\omega}$ and h_3.

core is given by (Phinney 1992)

$$\left(\frac{a}{c}\right)^{\text{Gal}} = \frac{\boldsymbol{a}_p \cdot \boldsymbol{n}}{c}$$
$$= -A_\odot \left[\cos b \cos l + \frac{\delta - \cos b \cos l}{1 + \delta^2 - 2\delta \cos b \cos l} \right], \quad (17)$$

where $R_0 = 8.122(31)$ kpc is the galactocentric distance of the Sun (Gravity Collaboration et al. 2018), l and b are the Galactic longitude and latitude, respectively, $\boldsymbol{a}_p$ is the pulsar acceleration vector, $\boldsymbol{n}$ is a unit vector pointing from the Solar system barycentre to the pulsar, and

$$A_\odot = \frac{V_c^2}{cR_0}, \quad (18)$$

where $V_c = 233.34(14)$ km s^{-1} is the Galactic rotation velocity (McGaugh 2018). For this, we estimate a contribution to $\dot{P}_b$ of $-1.23(15) \times 10^{-12}$ s s^{-1}.

The vertical component of the acceleration experienced by a pulsar at a Galactic altitude z is (Lazaridis et al. 2009)

$$\left(\frac{a}{c}\right)^z = -7.57 \times 10^{-20}|z| + 12.28 \times 10^{-20}\left(1 - e^{-4.31|z|}\right), \quad (19)$$

which is valid for pulsars at Galactic altitudes $|z| \lesssim 1.5$ kpc (Holmberg & Flynn 2004). For PSR J2045 + 3633, the Galactic altitude is -381 pc, well within the valid range, and we calculate a contribution to $\dot{P}_b$ of $-2.43(26) \times 10^{-14}$ s s^{-1}.

Putting these together, and taking into account the distance uncertainty, we find that all of the kinematic terms amount to $\dot{P}_b^{\text{kin}} = -0.60^{+0.01}_{-0.05} \times 10^{-12}$ s s^{-1}. This is consistent with the results of our timing analysis: with the DDFWHE model, we obtain $\dot{P}_b = +3.6(53) \times 10^{-12}$ s s^{-1}. From this, we conclude that we cannot yet detect the $\dot{P}_b$ expected from kinematic effects, and that the precision of $\dot{P}_b$ must be improved by more than an order of magnitude before measurement will be possible. This will be advantageous, as a measurement of the kinematic contribution to $\dot{P}_b$ would enable an accurate measurement of d.

A similar calculation is done for the spin period derivative, and the results are presented in Table 3.

3.7 The role of spin-orbit coupling

In Section 1.1, we mentioned that for systems consisting of two degenerate stars, we can generally assume that Newtonian perturbations to a Keplerian orbit can be neglected. However, this is not
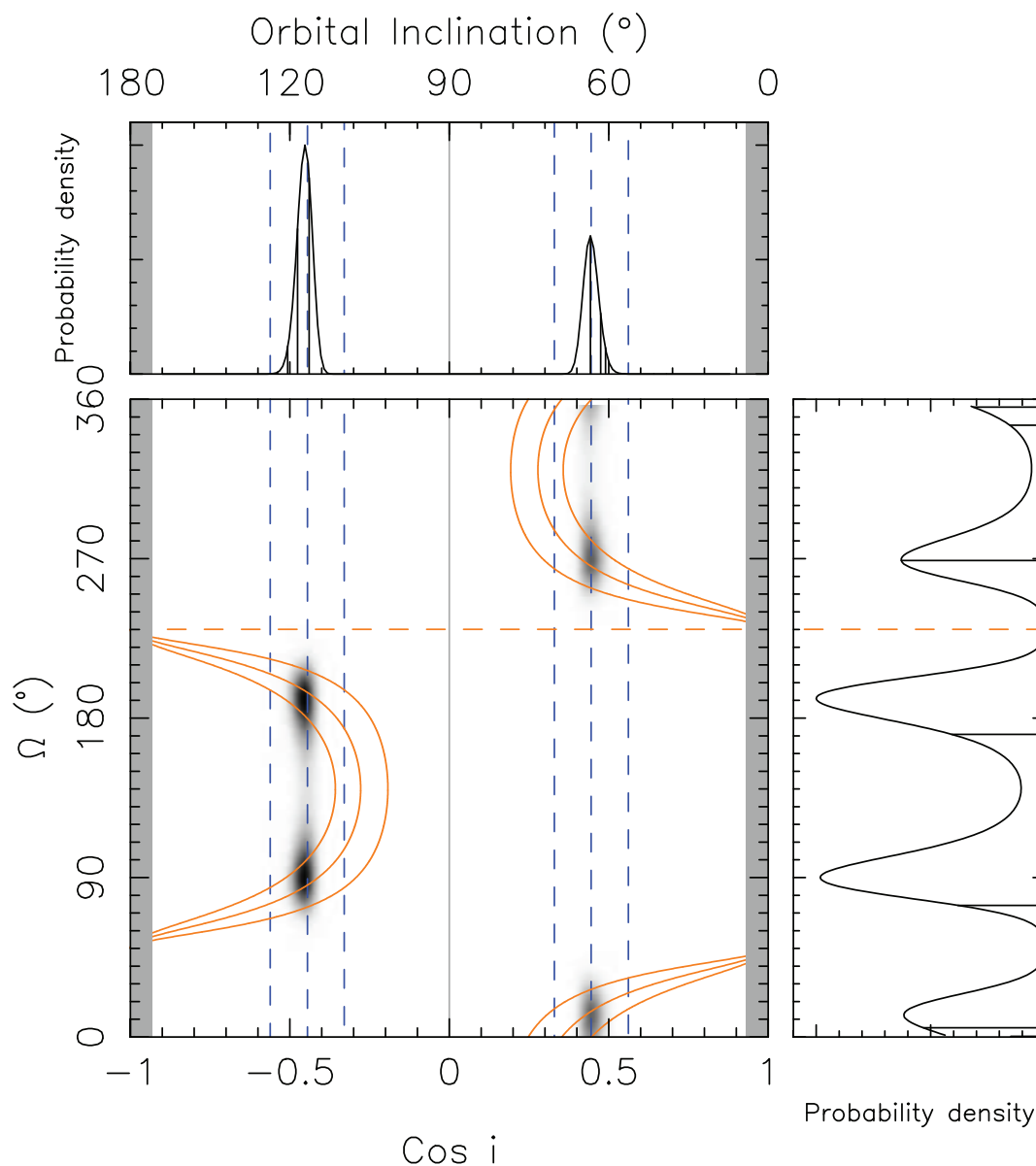
Figure 5. Constraints of the PSR J2045 + 3633 orbital line of nodes, as a function of the cosine of the orbital inclination. The grey shaded region is excluded by the mass function in combination with the estimate for the total mass. The dashed orange line indicates the PA of the proper motion (Θ_μ), and the curves with 1σ uncertainty regions are displayed for $\dot{x}$ (solid orange), and ς (dashed blue), obtained from the DDFWHE model. The greyscale colour maps show the likelihood from the χ^2 mapping analysis, and are from the same 3D map shown in Fig. 4; here with darker shades corresponding to a higher probability. The marginal plots show the 1D probability density functions for both axes. We can see that there are four main areas allowed by our timing analysis, which are well defined by the intersection of the cos i and $\dot{x}$ constraints. Currently, we cannot eliminate this degeneracy based on the timing alone, as the system is too distant for the detection of the annual orbital parallax which could break this degeneracy. Although the maximum likelihood occurs at $\Omega \sim 198°$ and cos $i \sim -0.45$, the polarimetry implies that the system has a positive cos i, which implies that one of the two positive cos i solutions is the correct one.

always the case. For PSR J1141 − 6545, a binary pulsar where the companion is a massive WD (Antoniadis et al. 2011), a change in the orbital inclination of the system was detected, by assuming the validity of GR for this system, i.e. by using the DDGR model (Venkatraman Krishnan et al. 2020). Such a change of inclination is caused (again, assuming the validity of GR) by classical and relativistic spin-orbit effects that result from the fast spin of the companion WD, which must have a spin period of only a few minutes. Although this anomalously fast spin of the companion WD is caused by the unusual evolutionary history of that system (the WD accreted matter from the progenitor to the pulsar), it

demonstrates that we must always be careful when making this assumption.

Evaluating these spin-orbit contributions for PSR J2045 + 3633 (Equations S7–S9 in Venkatraman Krishnan et al. 2020), we find that, even assuming a spin period of 2 min (the lower limit for the spin period of a spun-up WD like PSR J1141 − 6545), the maximum magnitudes of the classical and relativistic contributions to $\dot{x}$ are $\sim 6 \times 10^{-16}$ and $\sim -7 \times 10^{-16}$ lt-s s^{-1}, respectively. These are an order of magnitude smaller than our measured $\dot{x}$. In addition to this, unlike in the case of PSR J1141 − 6545, the WD companion to PSR J2045 + 3633 was not spun up by matter accreted from the progenitor to the pulsar. Instead, it was the pulsar that accreted matter

Table 5. Results of the χ^2 mapping with the DDK model for the two $\cos i$ regions (see the text).

$\cos i$ range	Best $\cos i$	Best Ω (°)	Best M ($M_\odot$)	Minimum χ^2
−0.9: −0.1	−0.45	190	2.13	5582.83
+0.1: +0.9	+ 0.45	269	2.13	5583.75

from the progenitor to the companion WD; we know this because the pulsar shows clear signs of having been recycled. For this reason, the WD will likely have a much slower rotation than the companion of PSR J1141 − 6545, and therefore the contribution of spin-orbit coupling to the observed $\dot{x}$ and $\dot{\omega}$ can be safely ignored.

3.8 χ^2 mapping

We can use all the constraints described above to determine the masses and the orbital orientation of the PSR J2045 + 3633 system in a self-consistent way. In order to do this, we use a χ^2 mapping technique similar to the one detailed in Stovall et al. (2019). In order to take into account the kinematic effects on all parameters (described in Kopeikin 1995, 1996, and which we discuss in Sections 3.3 and 3.5), we use the DDK orbital model, but in addition to this, assume the validity of GR. We map a 3D parameter space consisting of the total mass of the system (M), the cosine of the orbital inclination ($\cos i$), and the PA of the line of nodes (Ω). The reason for mapping along the M vector is that the total mass is well constrained by the $\dot{\omega}$ measurement of the system (see Section 3.3). The reason to map Ω and $\cos i$ is that this space is, for randomly aligned orbits, uniformly populated, and thus provides a flat prior.

For each point in this 3D space, the mass of the pulsar and the companion are known (via equation 2), and so we can calculate all PK parameters according to their GR equations and assume them in a trial DDK model, where they are held constant. The same is true for all of the kinematic effects (in particular, the secular and annual variations of x and ω), which are also completely determined for each point in this space. These are calculated within the DDK model from $\cos i$, Ω, the proper motion, and the assumed parallax (which is the inverse of the DM distance in kpc), without the need to specify $\dot{x}$. We then fit this model to the timing data by minimizing the residuals; for this, we allow all other timing parameters (i.e. the astrometric, spin, and Keplerian orbital parameters) to vary. A 3D probability density is then derived from the resulting χ^2 map.

Due to the degeneracy between i and $(180° − i)$ in the orbital inclination, we have sampled two different $\cos i$ regions: $[− 0°.9: −0°.1]$ and $[+ 0°.1: +0°.9]$, with steps of $0°.01$. Within both of these regions, we have sampled the Ω range $[0°: 359°]$ with steps of $1°$, and the M range of $[1.1\,M_\odot : 3.3\,M_\odot]$, with steps of $0.01\,M_\odot$. The results are summarized in Table 5.

From our χ^2 mapping results (Fig. 4), we have been able to infer very precise pulsar and companion masses of $m_p = 1.251^{+0.021}_{-0.021}\,M_\odot$ and $m_c = 0.873^{+0.016}_{-0.014}\,M_\odot$, respectively, and a total system mass of $M = 2.127^{+0.031}_{-0.031}\,M_\odot$, where all of our quoted uncertainties are 1σ. This represents an order of magnitude improvement in precision over the previously published value (Berezina et al. 2017). We are also able to constrain the orbital inclination i to two relatively narrow intervals: $63.8^{+1.5°}_{-1.6}$ and $117.5^{+1.6°}_{-1.5}$, which are much narrower than the estimate of ς. The precise masses and orbital inclination are described very well by the intersection of the $\dot{\omega}$ and h_3 constraints (see Fig. 4); they cannot be well described using the r–s parametrization of the Shapiro delay.

Although the two $\cos i$ intervals are relatively narrow, we are not able to well-constrain Ω, and we find four degenerate Ω-$\cos i$ solutions, albeit with the values corresponding to a negative $\cos i$ being approximately twice as likely, which can be seen in Fig. 5. The four possible Ω values are $9^{+13°}_{-20}$, $92^{+16°}_{-13}$, $187^{+13°}_{-13}$, and $272^{+16°}_{-13}$. The lower probability of a positive $\cos i$ is not statistically significant, and therefore our findings are consistent with the orbital inclination derived from the polarimetry of the pulsar by Berezina et al. (2017) and ourselves (Fig. 2, and see Section 3.4). Assuming a positive $\cos i$ to therefore be true, the results of the χ^2 mapping imply that $i = 63.8^{+1.5°}_{-1.6}$, and that the value of Ω is either $92^{+16°}_{-13}$ or $187^{+13°}_{-18}$.

Overall, the allowed regions in the Ω–$\cos i$ plane are well described by the narrow ranges of $\cos i$ determined by the intersection of $\dot{\omega}$ and h_3, and the constraints from the $\dot{x}$ measured in the DDFWHE solution. In order to determine which of the four combinations of Ω and $\cos i$ is correct purely from timing, we would need to measure the annual orbital parallax of the system (e.g. as Stovall et al. 2019 did for PSR J2234+0611). Given the large distance to PSR J2045 + 3633, the prospects for achieving this are not promising. It is clear though that continued timing will result in much improved values for $\dot{\omega}$ and $\dot{x}$, which will further improve the precision of the mass measurements and place tighter constraints on the regions of the Ω-$\cos i$.

4 DISCUSSION

4.1 Mass measurements

One of the main results of this work is the precise mass measurements of PSR J2045 + 3633 and its WD companion. We conclude that, given the $0.873^{+0.016}_{-0.014}\,M_\odot$ mass we have measured for the companion, it is likely to be a carbon–oxygen white dwarf (CO WD), and not an oxygen–neon–magnesium WD, i.e. the progenitor was not sufficiently massive for nuclear carbon burning to be initiated (Tauris, Langer & Kramer 2012). The $1.251^{+0.021}_{-0.021}\,M_\odot$ mass we have measured for PSR J2045 + 3633 is relatively low, and is evidence for very inefficient accretion of matter during the recycling phase, following its formation. Given that NSs are expected to be born with masses in excess of $\sim 1.15 − 1.20\,M_\odot$ (Tauris & Janka 2019, and references therein), this indicates that the pulsar accreted less than $\sim 0.10\,M_\odot$, despite significant mass-loss from the progenitor star of the $0.873\,M_\odot$ CO WD, which most likely had a ZAMS mass in excess of $4\,M_\odot$ (see e.g. fig. 1 in Tauris, Langer & Kramer 2011).

To further put the masses of PSR J2045 + 3633 and its companion into perspective, in Fig. 6, we plot all currently known precise masses measured for pulsar–WD systems. In this plot, we can see several striking trends. First, most systems fall into two well-defined populations. The first corresponds to systems with Helium WD (HeWD) components, which have a narrow distribution of WD masses (which are mostly correlated with the orbital period of the system, as described by Tauris & Savonije 1999). The second population has a surprisingly narrow range of companion CO WD masses, from 0.7 to 0.9 $M_\odot$, and these masses are not correlated with the orbital period. PSR J2043+3633 is clearly within this latter class, and this work provides the best-measured masses of systems that are within this group. Another member of this class with a well-known mass, PSR J2053 + 4650, was studied in detail in the same work that announced the discovery of PSR J2045 + 3633 (Berezina et al. 2017).

There is a relative dearth of WD masses between 0.41 and 0.7 $M_\odot$. This gap is partly observational: according to the Tauris & Savonije (1999) relation between the orbital period of a pulsar-HeWD binary and the HeWD mass, we expect the upper end of this range (up to 0.46 $M_\odot$) to be populated exclusively by pulsar-HeWD binaries in
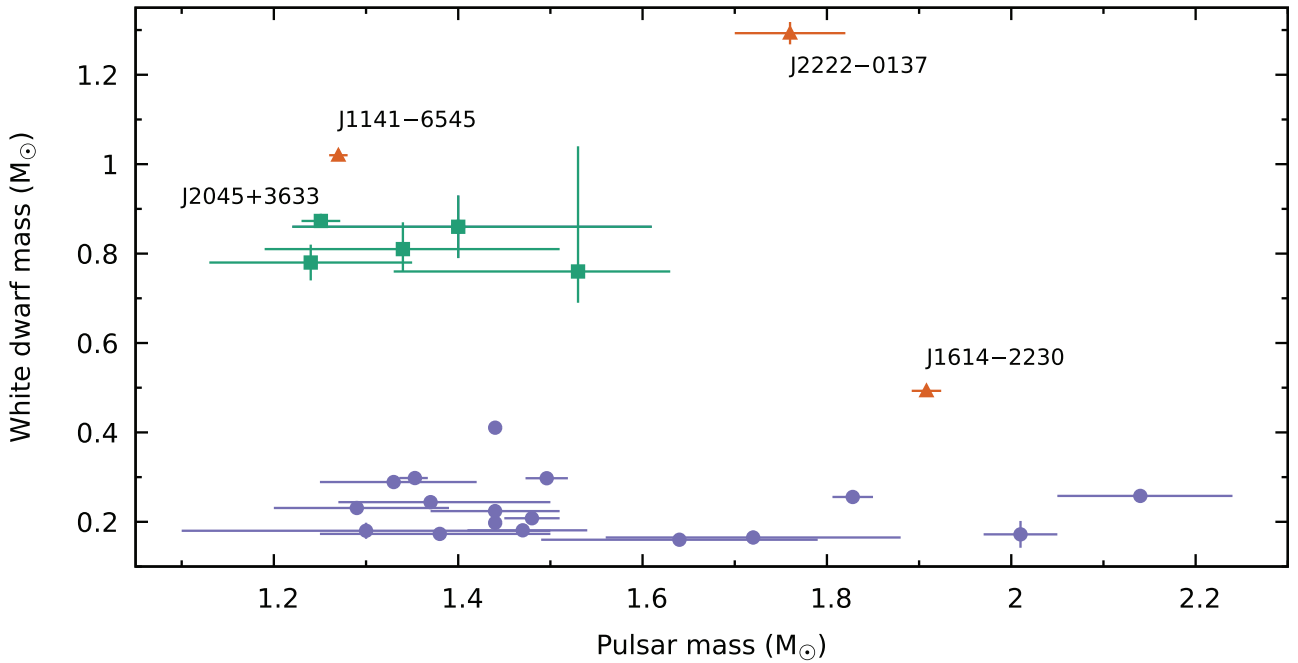
Figure 6. Masses of all known pulsar–WD systems with precise mass measurements that are not located in globular clusters. The systems with (low-mass) helium white dwarf (HeWD) companions are shown as purple circles, and the systems with massive white dwarf (CO WD) companions are shown as green squares. With the exception of three special cases, which are highlighted (orange triangles: PSR J1141 − 6545, where the WD formed first and thus the pulsar is not recycled, and the unusual systems J1614 − 2230 and J2222 − 0137, discussed in the text), all systems fall into two distinct populations. The systems with CO WDs mostly appear within a narrow range of pulsar and WD masses.

orbits with periods in excess of a few hundreds of days. The observed distribution of mass functions suggests that this is indeed the case. However, the lack of precisely measured WD and pulsar masses with such wide orbits is caused by the fact that, for those wide orbits, pulsar recycling is inefficient and produces pulsars with relatively short-lived radio emission (i.e. due to insufficient decay of the remaining magnetic field, the spin-down torque is large), and with spin periods of many tens of milliseconds. For those slow-spinning pulsars, the achievable timing precision is generally not sufficiently high for the precise detection of the Shapiro delay signature. Furthermore, with large orbital periods, there are potentially large variations in DM during the long orbital cycle, which further complicates Shapiro delay measurements.

A slow spin period is also an issue for pulsars with massive WD companions, since the massive progenitor to the WD evolves rapidly and the recycling process is relatively short. However, as is the case for PSR J2045 + 3633, some of these systems have a measurable $\dot{\omega}$ which, together with low-precision detections of the Shapiro delay, allows precise masses to be determined. The $\dot{\omega}$ cannot be measured for pulsar-HeWDs with orbits of many hundreds of days.

The range of pulsar masses with HeWD companions appears to be distinctively larger than that of pulsars with more massive CO WD companions between 0.7 and 0.9 $M_\odot$. It is interesting to speculate on possible causes for this. One possibility is that the progenitors of HeWDs have a much slower evolution; in these cases, the accretion episode that is observable as a low-mass X-ray binary phase is very long-lived. This results in much faster spin periods for the pulsars in this class compared to the pulsars with more massive companions (see e.g. figs 3 and 9 in Tauris et al. 2012), and this could also result in much larger accreted masses.

Mass transfer between two stars via Roche lobe overflow (RLO) can be initiated while the donor star is still on the main-sequence

(Case A RLO), during hydrogen shell burning (Case B RLO) or during helium shell burning (Case C RLO). The corresponding evolutionary time-scales for these different cases will in general proceed on a nuclear, thermal, or dynamical time-scale, respectively, or a combination thereof. The progenitor systems of pulsar-CO WD binaries are thought to be intermediate-mass X-ray binaries (IMXBs), with typical donor star masses of 3 to 6 $M_\odot$. Only a small fraction of these will undergo RLO Case A (during hydrogen core burning), as few such binaries are formed in the narrow orbital range that is required for this scenario. A rare example of this scenario being met is PSR J1614 − 2230 (Tauris et al. 2011), which resulted in the formation of a 0.493(3) $M_\odot$ CO WD, the only in the gap between 0.41 and 0.7 $M_\odot$. This is a massive pulsar (Demorest et al. 2010; Arzoumanian et al. 2018) that has an unusually fast spin for a system with such a massive WD companion. The prolonged mass transfer associated with Case A RLO provides a good explanation of these unusual characteristics.

Case B (and C) RLO covers a very wide range of orbital periods, such that the donor star cores can grow to a larger mass, consistent with the observed 0.7 to 0.9 $M_\odot$ range (see fig. 1 of Tauris et al. 2011). Combined with the initial mass function, it is perhaps reasonable that few very massive WDs are expected, which is consistent with the observed population.

In addition to PSR J1614 − 2230, there are two unusual pulsar-WD binary systems that do not fall in these two populations (highlighted with orange triangles in Fig. 6). The first one, PSR J1141 − 6545, had a rather unusual evolution, where the WD formed first and accreted matter from the progenitor of the pulsar, spinning up significantly in the process (Venkatraman Krishnan et al. 2020). After that, the secondary exploded in a supernova, forming a normal pulsar which can not be recycled and therefore remains in an eccentric orbit. Currently, there are at most two other systems that are thought to

have followed a similar evolution (see Ng et al. 2018, and references therein). The second unusual system is J2222 − 0137, which has an unusually massive ($\sim 1.3\,M_\odot$) WD companion, and is the most massive double-degenerate binary system currently known ($3.06\,M_\odot$, Cognard et al. 2017).

To summarize, the observed masses of components in pulsar-WD binaries are consistent with there being two main groups: The pulsar-HeWD systems, where the companion mass is determined by the orbital period of the system and the range of pulsar masses is quite broad, and a second group of systems with massive WDs that has a rather narrow range of pulsar and WD masses, with the latter all falling within 0.7 to $0.9\,M_\odot$. In addition to these two main groups, there are likely several other groups with different evolutionary histories and (presumably) much smaller populations. A possible exception is the group of systems with very high-mass WDs, such as PSR J2222 − 0137. This is the sole member of that class with a well-measured mass. However, it is located only 267 pc from our Solar System, and this proximity implies that there are probably many more systems like this in the Galaxy i.e. that this class is potentially much more numerous.

4.2 Transverse velocity

The PSR J2045 + 3633 transverse velocity of $109(22)\,\mathrm{km\,s^{-1}}$ is calculated in a heliocentric reference frame. In order to derive further conclusions, we first need to estimate its velocity relative to the local standard of rest (LSR). To do this, we follow the procedure highlighted by Zhu et al. (2019).

For an object at the position of the pulsar that is in the LSR, we expect a horizontal proper motion of $-5.39\,\mathrm{mas\,yr^{-1}}$, and a vertical proper motion of $-0.28\,\mathrm{mas\,yr^{-1}}$. Subtracting these values from the horizontal and vertical components of the observed proper motion, we obtain the peculiar proper motion: $+1.30$ and $+1.09\,\mathrm{mas\,yr^{-1}}$ along the horizontal and vertical directions, respectively, i.e. the total peculiar proper motion is around $1.70\,\mathrm{mas\,yr^{-1}}$. This corresponds to a transverse peculiar velocity of $44(9)\,\mathrm{km\,s^{-1}}$, which is relatively small in comparison to most other pulsars, in particular binary pulsars. There are other members of the pulsar-massive WD class that are known to have very low peculiar velocities. Two examples are PSR J1802 − 2124 (Ferdman et al. 2010) and PSR J1949 + 3106; the latter has a tangential peculiar velocity smaller than $10\,\mathrm{km\,s^{-1}}$ (Zhu et al. 2019). More broadly, the pulsars with massive WDs seem to have a smaller range of Galactic heights, which is consistent with having lower peculiar velocities (Ng et al. 2014; Parent et al. 2019). This can generally be interpreted as the result of the 'anchoring' effect of a more massive companion at the time of the supernova that forms the pulsar i.e. the more massive the companion, the smaller the change of velocity for the system after the supernova (from conservation of momentum). An additional effect would be if the progenitors of these more massive WDs were more efficient in stripping off the envelope of the progenitors to the pulsars, as such stripped supernovae are likely to have experienced smaller associated kicks (see discussions in Tauris, Langer & Podsiadlowski 2015, and references therein).

4.3 Binary evolution

As the PSR J2045 + 3633 orbit is relatively circular and the pulsar is recycled, albeit only partially ($P = 31.7\,\mathrm{ms}$, $\dot{P} = 5.8847(3)^{-19}\,\mathrm{s\,s^{-1}}$), this indicates that mass transfer occurred after the formation of the pulsar, and therefore the companion formed second. The large mass

of the WD companion implies that it would have formed from an asymptotic giant branch (AGB) star.

Pulsar-CO WD binaries are usually thought to form via two evolutionary channels (Tauris et al. 2012): stable RLO in an IMXB, and common envelope (CE) evolution. Recent work by Misra et al. (2020) on stable RLO from IMXB systems demonstrates that it is difficult to produce a binary with the component masses and orbital period that we measure, which makes formation via CE evolution the more likely scenario.

The radius of the progenitor star can be estimated from models relating the core mass to the radius. Using the models presented in van der Sluys, Verbunt & Pols (2006), we estimate the stellar radius of the progenitor to be $\sim 400\,R_\odot = 928$ lt-s i.e. approximately an order of magnitude greater than the current size of the orbit ($55\,R_\odot = 127.6$ lt-s, calculated from Kepler's third law in Section 3.3). Therefore after the companion star evolved to the AGB phase, the system must have gone through a CE phase, during which in-spiralling occurred (e.g. Paczynski 1976; Iben & Livio 1993); a scenario which is consistent with the pulsar being only partially recycled. We note, however, that the van der Sluys et al. (2006) model are not directly applicable to this system, and we use them here only to obtain a general estimate of the progenitor radius.

For such a formation scenario, it is perhaps unexpected that the orbit is still as wide as it is, and with a relatively large eccentricity. Binary systems that are thought to form following a CE phase typically have orbital periods ~ 1–10 d, and much lower eccentricities (see e.g. Taam, King & Ritter 2000). Logically, there are three possible explanations for this:

(i) The system was initially highly eccentric, and was later stabilized at some point in its evolution.

(ii) The system was initially more circular, and eccentricity was induced at some point in the binary evolution.

(iii) The system was initially moderately eccentric, and much of that eccentricity remains.

Below, we suggest possible scenarios that could arise from points (i)–(iii):

4.3.1 Stabilized orbit: equilibrium from fluctuation dissipation

Low-mass binary pulsars (i.e. those with HeWD companions) typically have a small but non-zero eccentricity, as the envelope of the red giant branch star progenitor of the companion is convective, and therefore has a non-zero and variable quadrupole moment (Phinney 1992). A statistical relation was found to exist between eccentricity and orbital period for these systems (Phinney & Kulkarni 1994), which is invalid for binaries with higher mass companions (e.g. CO WDs), which will have a different structure at the point where they detach. While the Phinney (1992) process does not apply to binaries with high-mass WD companions, these systems do appear to have a preference for higher eccentricities and longer periods in higher mass systems, which could indicate that a similar process occurs during their evolution.

4.3.2 Induced eccentricity

It is possible that the orbit was circularized in the post-CE phase, but some process-induced eccentricity later in the evolution of the system. This could perhaps be somewhat similar to the process described by Antoniadis (2014) for eccentric pulsar-HeWD binaries, where late in the evolution, a large final flash expels material

from a proto-HeWD companion into a circumbinary disc, which induces eccentricity. Though this model cannot work directly for PSR J2045 + 3633, since here a helium shell flash would be needed when producing a CO WD, and it remains to be shown if such a scenario is possible.

Related to this scenario, eccentricity could have been induced in the post-CE phase through interaction with a post-AGB phase circumbinary dust ring remnant, through the process described by Dermine et al. (2013). This scenario would imply that the CE triggered by AGB phase was the last stage of mass transfer in the evolution of the system (i.e. there was no naked helium giant phase, so-called Case BB RLO).

4.3.3 Leftover eccentricity: rapid common envelope phase

A short CE phase in the binary evolution would not allow enough time for the binary to be circularized through friction in the envelope, and would account for the pulsar being only partially recycled (see Tauris et al. 2012 for a similar hypothesis for PSR J1822 − 0848). We now investigate this hypothesis as a proof of concept by using simple arguments and our measurements of the pulsar and WD masses, and the orbital separation.

Earlier, we estimated the stellar radius of the AGB star to be $\sim 400 R_\odot = 928$ lt-s, using the models presented in van der Sluys et al. (2006). We also use the measured WD mass to estimate a progenitor AGB star mass of roughly $\sim 4.9 M_\odot$ using the models presented in Karakas, Lattanzio & Pols (2002). If we assume that the Roche lobe radius is equal to the radius of the AGB star, this allows us to estimate the initial separation a_i of the binary components using (Eggleton 1983)

$$R_{rl} = \frac{0.49 q^{2/3}}{0.6 q^{2/3} + \ln(1 + q^{1/3})} \, a_i, \qquad (20)$$

where $q = M_1/M_2$ is the mass ratio (donor star mass to accretor star mass), i.e. we use $q = 4.9/1.25$. Using this, we estimate an initial component separation $a_i = 800 R_\odot = 1857$ lt-s.

We can test this scenario by comparing the energy required to unbind the CE to the initial and final orbital binding energies. The change in orbital energies is given by

$$\Delta E_{orbit} = \frac{G M_{wd} M_{psr}}{2 a_f} - \frac{G M_{agb} M_{psr}}{2 a_i}, \qquad (21)$$

and taking the final orbital separation as our measured value of the PSR J2045 + 3633 orbital semimajor axis, $a_f = 55 R_\odot = 127.6$ lt-s, we estimate a change in orbital energy $\Delta E = 2.31 \times 10^{46}$ erg. The CE binding energy is given by (de Kool 1990)

$$E_{bind} = \frac{G M_{agb} M_{wd}}{\lambda R_{rl}}, \qquad (22)$$

where λ is a numerical value that is often (but not always) of order unity, which accounts for the structure of the star, and is usually either left as a free parameter or estimated through detailed modelling (see e.g. Dewi & Tauris 2000; Ivanova et al. 2013). Assuming $\lambda = 1$ and using our earlier values, we estimate a value for the CE binding energy $E_{bind} = 2.02 \times 10^{46}$ erg. This is remarkably close to our estimate of the change in orbital energy during the in-spiral, and the two values can be made to fit by setting $\lambda = 0.87$, and assuming 100 per cent efficiency in the conversion of released orbital energy into kinetic energy to expel the CE.

Although merely based on simplified energy considerations and disregarding additional effects such as released recombination energy, accretion energy and, not least, a detailed donor star structure

(see Ivanova et al. 2013 for a review), we conclude that this CE scenario could be possible. The expected outcome would indeed be a large reduction in orbital separation, and a mildly recycled pulsar in a non-zero eccentric orbit due to rapid in-spiral.

We note that a more realistic model of the λ parameter for evolved (giant) stars predicts values much larger than unity ($\lambda \sim 10$ for $4-5 M_\odot$ stars at $R \sim 400 R_\odot$, Dewi & Tauris 2000), which would significantly lower the binding energy of the CE and facilitate its ejection and the proposed scenario. A thorough evaluation of the orbital evolution is beyond the scope of our work.

5 CONCLUSIONS AND PROSPECTS

Using 6 yr of radio timing data, we have made precise mass measurements of PSR J2045 + 3633 and its WD companion, and have placed further constraints on its orbital geometry. The data set we have used in this work has allowed an order of magnitude improvement over the previously published masses.

We have examined the mass–mass distribution of Galactic pulsar-WD systems, and find evidence for most systems with precisely measured masses belonging to two distinct populations; one of them, the class with CO WD companions to which PSR J2045 + 3633 belongs, with a surprising narrow range of WD masses. Using our measurements of the masses and orbital parameters, we have proposed scenarios for the evolutionary history of this binary system, and conclude that a rapid CE phase is the most likely formation scenario.

Continued timing will greatly improve the measurements of the PK parameters, particularly $\dot{\omega}$ and $\dot{x}$. This will yield much improved mass estimates for this system, and significantly reduce the sizes of the allowed regions of the Ω–$\cos i$ plane (Figs 4 and 5), but it is not clear whether this will allow the degeneracy to be eliminated between the four Ω and $\cos i$ solutions, based on timing alone. Two of those solutions can, in principle, be eliminated based on the results of the RVM fit to the polarimetric data of the pulsar.

As this pulsar is distant, we have not been able to measure a parallax from the timing, meaning that many of the derived quantities which rely on distance are only estimates. However, the continued and relatively fast improvement of $\dot{P}_b$ will eventually yield a precise distance (e.g. Bell & Bailes 1996). Together with the improvement in the measurement of the proper motion, this will yield much improved estimates of the velocity of the system. All of these will be useful to improve our models of the evolution of the binary.

at Effelsberg. We thank the anonymous referee for their very helpful comments, which have improved how our work is presented here.

DATA AVAILABILITY

The data underlying this paper will be shared on a reasonable request to the corresponding author.

REFERENCES

Alam M. F. et al., 2020, preprint(arXiv:2005.06495)

Alpar M. A., Cheng A. F., Ruderman M. A., Shaham J., 1982, Nature, 300, 728

Anderson D., Freire P., Yunes N., 2019, Class. Quantum Gravity, 36, 225009

Antoniadis J., 2014, ApJ, 797, L24

Antoniadis J., Bassa C. G., Wex N., Kramer M., Napiwotzki R., 2011, MNRAS, 412, 580

Antoniadis J. et al., 2013, Science, 340, 448

Antoniadis J., Tauris T. M., Ozel F., Barr E., Champion D. J., Freire P. C. C., 2016, preprint(arXiv:1605.01665)

Archibald A. M. et al., 2018, Nature, 559, 73

Arzoumanian Z. et al., 2018, ApJS, 235, 37

Barr E. D. et al., 2013, MNRAS, 435, 2234

Bassa C. G. et al., 2016, MNRAS, 456, 2196

Bell J. F., Bailes M., 1996, ApJ, 456, L33

Berezina M. et al., 2017, MNRAS, 470, 4421

Cognard I. et al., 2017, ApJ, 844, 128

Cordes J. M., Lazio T. J. W., 2002, preprint(arXiv:e-print)

Cromartie H. T. et al., 2020, Nat. Astron., 4, 72

Damour T., 2015, Class. Quantum Gravity, 32, 124009

Damour T., Deruelle N., 1985, Ann. Inst. H. Poincaré (Physique Théorique), 43, 107

Damour T., Deruelle N., 1986, Ann. Inst. H. Poincaré (Physique Théorique), 44, 263

Damour T., Taylor J. H., 1992, Phys. Rev. D, 45, 1840

de Kool M., 1990, ApJ, 358, 189

Demorest P. B., Pennucci T., Ransom S. M., Roberts M. S. E., Hessels J. W. T., 2010, Nature, 467, 1081

Dermine T., Izzard R. G., Jorissen A., Van Winckel H., 2013, A&A, 551, A50

Desvignes G. et al., 2016, MNRAS, 458, 3341

Dewi J. D. M., Tauris T. M., 2000, A&A, 360, 1043

Donner J. Y. et al., 2019, A&A, 624, A22

Eggleton P. P., 1983, ApJ, 268, 368

Ferdman R. D. et al., 2010, ApJ, 711, 764

Folkner W., Jacobson R. A., Park R., Williams J. G., 2016, in AAS/Division for Planetary Sciences Meeting Abstracts #48, AAS/Division for Planetary Sciences Meeting Abstracts. p. 120.07

Fonseca E., Stairs I. H., Thorsett S. E., 2014, ApJ, 787, 82

Freire P. C. C., Wex N., 2010, MNRAS, 409, 199

Freire P. C. C. et al., 2011, MNRAS, 412, 2763

Freire P. C. C. et al., 2012, MNRAS, 423, 3328

Gravity Collaboration et al., 2018, A&A, 615, L15

Holmberg J., Flynn C., 2004, MNRAS, 352, 440

Hotan A. W., van Straten W., Manchester R. N., 2004, PASA, 21, 302

Iben, Icko J., Livio M., 1993, PASP, 105, 1373

Ivanova N. et al., 2013, A&A Rev., 21, 59

Karakas A. I., Lattanzio J. C., Pols O. R., 2002, PASA, 19, 515

Kopeikin S. M., 1995, ApJ, 439, L5

Kopeikin S. M., 1996, ApJ, 467, L93

Kramer M. et al., 2006, Science, 314, 97

Kramer M., Stairs I., Venkatraman Krishnan V., 2020, MNRAS

Lattimer J. M., Prakash M., 2001, ApJ, 550, 426

Lazaridis K. et al., 2009, MNRAS, 400, 805

Lazarus P., Karuppusamy R., Graikou E., Caballero R. N., Champion D. J., Lee K. J., Verbiest J. P. W., Kramer M., 2016, MNRAS, 458, 868

Liu K. et al., 2014, MNRAS, 443, 3752

Lorimer D. R., 2008, Living Rev. Relativ., 11, 8

Lorimer D. R., Kramer M., 2005, Handbook of Pulsar Astronomy. Cambridge Univ. Press, Cambridge

Martinez J. G. et al., 2015, ApJ, 812, 143

McGaugh S. S., 2018, Res. Notes Am. Astron. Soc., 2, 156

Misra D., Fragos T., Tauris T., Zapartas E., Aguilera-Dena D. R., 2020, A&A, 642, A174

Ng C. et al., 2014, MNRAS, 439, 1865

Ng C. et al., 2018, MNRAS, 476, 4315

Paczynski B., 1976, in Eggleton P., Mitton S., Whelan J., eds, IAU Symp., Vol. 73, Structure and Evolution of Close Binary Systems, Kluwer Academic, Springer, Dordrecht, The Netherlands. p. 75

Parent E. et al., 2019, ApJ, 886, 148

Peters P. C., Mathews J., 1963, Phys. Rev., 131, 435

Phinney E. S., 1992, Royal Society of London., 341, 39

Phinney E. S., Kulkarni S. R., 1994, ARA&A, 32, 591

Radhakrishnan V., Cooke D. J., 1969, Ap. Lett., 3, 225

Shaifullah G. et al., 2016, MNRAS, 462, 1029

Shao L., Sennett N., Buonanno A., Kramer M., Wex N., 2017, Phys. Rev. X, 7, 041025

Shapiro I. I., 1964, PRL, 13, 789

Shklovskii I. S., 1970, Soviet Ast., 13, 562

Stairs I. H., 2003, Living Rev. Relativ., 6, 5

Stovall K. et al., 2019, ApJ, 870, 74

Taam R. E., King A. R., Ritter H., 2000, ApJ, 541, 329

Tauris T. M., Janka H.-T., 2019, ApJ, 886, L20

Tauris T. M., Savonije G. J., 1999, A&A, 350, 928

Tauris T. M., Langer N., Kramer M., 2011, MNRAS, 416, 2130

Tauris T. M., Langer N., Kramer M., 2012, MNRAS, 425, 1601

Tauris T. M., Langer N., Podsiadlowski P., 2015, MNRAS, 451, 2123

Tauris T. M. et al., 2017, ApJ, 846, 170

Taylor J. H., Weisberg J. M., 1982, ApJ, 253, 908

van der Sluys M. V., Verbunt F., Pols O. R., 2006, A&A, 460, 209

Venkatraman Krishnan V. et al., 2020, Science, 367, 577

Voisin G., Cognard I., Freire P. C. C., Wex N., Guillemot L., Desvignes G., Kramer M., Theureau G., 2020, A&A, 638, A24

Weisberg J. M., Huang Y., 2016, ApJ, 829, 55

Weisberg J., Taylor J., 1981, Gen. Relativ. Gravit., 13, 1

Wex N., 2014, preprint(arXiv:1402.5594)

Yao J. M., Manchester R. N., Wang N., 2017, ApJ, 835, 29

Zhu W. W. et al., 2019, ApJ, 881, 165

Özel F., Freire P., 2016, ARA&A, 54, 401

This paper has been typeset from a TₑX/LATₑX file prepared by the author.